UNIVERSITY OF CALIFORNIA, IRVINE

1-D Heat Conduction in Porous Layers for Electrochemical Energy Conversion

THESIS

Submitted in partial satisfaction of the requirements for the degree of

MASTER OF SCIENCE

in Chemical and Biomolecular Engineering

by

Walther Villatoro

Thesis Committee:

Assistant Professor Iryna Zenyuk, Chair

Chancellor's Professor Plamen Atanassov

Assistant Professor Yoonjin Won

2020

TABLE OF CONTENTS

LIST OF FIGURES

LIST OF TABLES

ACKNOWLEDGEMENTS

I would like to thank my advisor, Dr. Iryna Zenyuk, for giving me the opportunity to conduct research in her group, always providing great guidance, and for tomography data.

I would also like to acknowledge IRD Fuel Cells for providing the funding for this research.

Thank you Ying, for helping with the tomography data and David Morales, for initial experimental setup design. The pore-size distributions for X-ray tomography samples were done by Ben Zackin, a former Tufts student.

Finally, thank you Deeanna, for all the help and support along the way.

ABSTRACT OF THE THESIS

1-D Heat Conduction in Porous Layers for Electrochemical Energy Conversion

By

Walther Villatoro

Master of Science in Chemical and Biomolecular Engineering

University of California, Irvine, 2020

Assistant Professor Iryna Zenyuk, Chair

Polymer electrolyte fuel cells (PEFCs) and electrolyzers show promise in enabling renewable energy source technologies such as solar and wind. Thermal management is an important aspect in the operation of these devices because it can have adverse effects on performance and durability. The porous transport layers (PTLs)/gas diffusion layers (GDLs) are porous thin layers that have many functions in both electrolyzers and fuel cells. One of their functions is to uniformly distribute heat, whereas the function of the porous flow fieldsis to distribute fluids. Knowledge of the thermal conductivity of these components is necessary when optimizing heat transport and modeling thermal distributions in PEFCs and electrolyzers. To this end, the through-plane effective thermal conductivity of a sintered and fiber titanium PTL, carbon based GDL, and nickel chromium flow field mesh is investigated *ex-situ* for the first time through experimental work for all the materials and computed tomography for the PTLs.

Fourier's law was used to calculate thermal conductivity through a steady-state method. An apparatus was built and designed to measure the heat flux through layers of an individual sample and temperatures at designated points. The effective thermal conductivity of the dry, wet, and tomography calculated sintered Ti PTL is 0.46 ± 0.21 $Wm^{-1}K^{-1}$, 0.91 ± 0.10 $Wm^{-1}K^{-1}$, 7.66 $Wm^{-1}K^{-1}$, respectively. For the fiber Ti PTL, measured values are 0.41 ± 0.07 $Wm^{-1}K^{-1}$, 0.78 ± 0.46 $Wm^{-1}K^{-1}$, and 5.22 $Wm^{-1}K^{-1}$. The effective thermal conductivity of the GDL is 0.32 ± 0.05 $Wm^{-1}K^{-1}$

and 0.17 ± 0.03 $Wm^{-1}K^{-1}$ for the NiCr porous flow field mesh. It is shown that the thermal conductivity of the PTLs increases by a larger amount than expected when water is present. The studies presented here illustrate the importance of continued work in thermal characterization of the porous materials used in electrochemical energy conversion and storage.

1 INTRODUCTION

In an electricity driven society, finding a sustainable energy source is a priority. There are multiple resources that can be used as energy sources and also as energy conversion resources to provide power and currently the most widely used are still fossil fuels. Others are biomass and biogas, hydro, wind, and solar. Sustainability requires that resources be naturally replenished at the same rate at which they are used[1]. Replenishment of fossil fuels takes millions of years, months to years for biomass and biogas, weeks to months for hydro, days to weeks for wind, and instantaneous for solar[2]. Solar and wind power are the most sustainable resources available, however their natural fluctuation cause intermittency[3]. Due to the intermittency of renewables, a need for energy storage and clean power conversion is necessary.

Hydrogen is a suitable option for energy storage because of its high gravimetric energy density[4]. The excess energy generated from fluctuating renewables like solar and wind can be used to make hydrogen and oxygen via water electrolysis[1,5]. Water electrolysis produces hydrogen of almost 100% purity[6]. Utilization of energy from renewables for water electrolysis serves to produce hydrogen without harmful emissions, while at the same time providing reliable power since hydrogen can be used as fuel[7].

Hydrogen generated via electrolysis can then be stored as compressed gas or liquid hydrogen and then transported through natural gas pipelines and deployed in a location of need. It can be combusted at high temperature, or used within fuel cells to be converted back to electricity. Fuel cells convert chemical energy directly into electricity by reacting hydrogen with oxygen and producing only water[8]. Therefore, the high purity hydrogen generated via water electrolysis can be utilized in fuel cells to produce electricity without emitting greenhouse gases[3,9]. The polymer electrolyte fuel cell (PEFC) is a high-performance fuel cell which efficiently harnesses the energy from hydrogen-oxygen electrochemical reactions[4,10]. PEFCs are ideal for

uses such as transportation because they operate at temperatures lower than 90°C while still maintaining high power density[8].

A typical PEFC is composed of two compartments that are separated by an electrolyte membrane that transports protons from the anode side to the cathode side and also electrically separates anode from cathode[8]. The electrolyte membrane is part of the membrane electrode assembly (MEA) which includes catalyst layers, and gas diffusion layers (GDLs) with a microporous layer (MPL) that improves contact between the GDL and catalyst layers[11,12]. The MEA is placed between bipolar plates that generally have flow channels machined on the side facing the MEA[13]. The purpose of bipolar plates is to redistribute reactant gases, and to enable electric contact to the catalyst layers. Bipolar plates are also made of thermally conductive materials to remove the heat from the fuel cell Figure 1 shows how the materials are combined in a fuel cell.

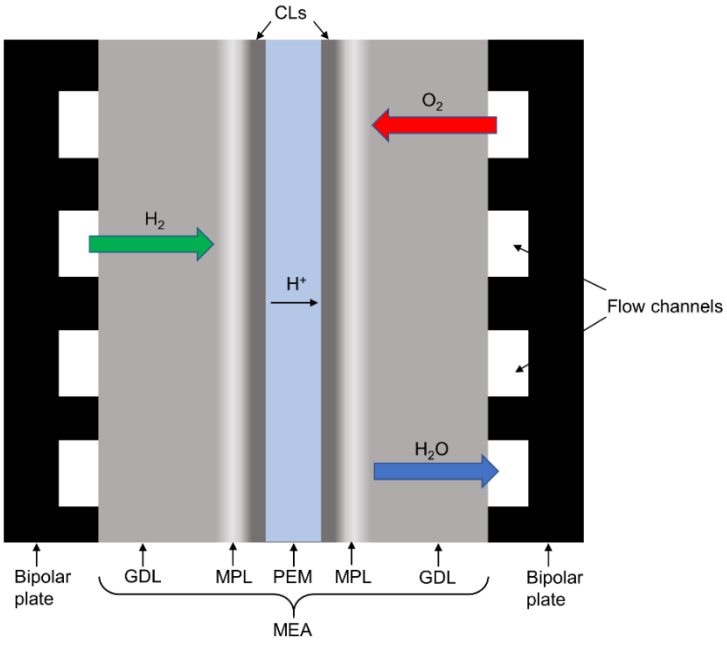

Figure 1: Schematic diagram of a PEFC depicting the polymer electrolyte membrane (PEM), catalyst layers (CLs), micro-porous layers (MPL), gas diffusion layers (GDL), and bipolar plates

which serve as supports for the flow fields. H_2 enters through the anode side and O_2 through the cathode side. H_2O is produced in the cathode side removed by the GDL into the flow channels.

Hydrogen gas is introduced to the anode and oxidized, splitting into electrons and protons. The energy conversion is achieved through the electrochemical reactions of hydrogen and oxygen[8]:

$$H_2 \rightarrow 2H^+ + 2e^- \qquad \text{anode}$$

$$\frac{1}{2}O_2 + 2H^+ + 2e^- \rightarrow H_2O \qquad \text{cathode}$$

$$\frac{1}{2}O_2 + H_2 \rightarrow H_2O \qquad \text{overall}$$

The separation of reactions is essential as it forces the electrons to travel from the anode to the cathode through an external circuit while the protons pass through the electrolyte membrane. The flow of electrons through the external circuit subsequently creates an electrical current. On the cathode side, the protons and electrons react with oxygen to produce heat and water[8,14].

Water electrolysis is accomplished using electrolyzers. Proton exchange membrane (PEM) electrolyzers are of interest because they feature high dynamic range, fast load change capability, production of high purity hydrogen, high pressure differential operability, and ability to reach high current density, up to 20 Acm^{-2}, while maintaining higher efficiency than alkaline and solid oxide electrolyzers[15]. Mockl et. al.[15] reported an efficiency of 61 % based on lower heating value for a PEM electrolyzer operating at 10 Acm^{-2}. PEM electrolyzers use electricity to produce hydrogen and oxygen from water. Oxygen evolution occurs on the anode side while hydrogen evolution occurs on the cathode side and can be expressed as:

$$H_2O \rightarrow \frac{1}{2}O_2 + 2H^+ + 2e^- \qquad \text{anode}$$

$$2H^+ + 2e^- \rightarrow H_2 \qquad \text{cathode}$$

The overall reaction in water electrolysis is:

$$H_2O \rightarrow \frac{1}{2}O_2 + H_2 \qquad \text{overall}$$

PEM electrolyzers are constructed similar to PEFCs. They consist of an MEA placed between two bipolar plates. However, the materials used for the transport layers are different due to the systems serving different purposes and having different operating conditions[12]. Electrolyzers use titanium bipolar plate on the anode and titanium-based porous transport layers (PTLs) without an MPL in the anode instead of carbon paper[12]. A carbon based PTL is still used in the cathode because it is not subjected to a corrosive environment. Figure 2 shows how the materials in a PEM electrolyzer are combined to make a cell.

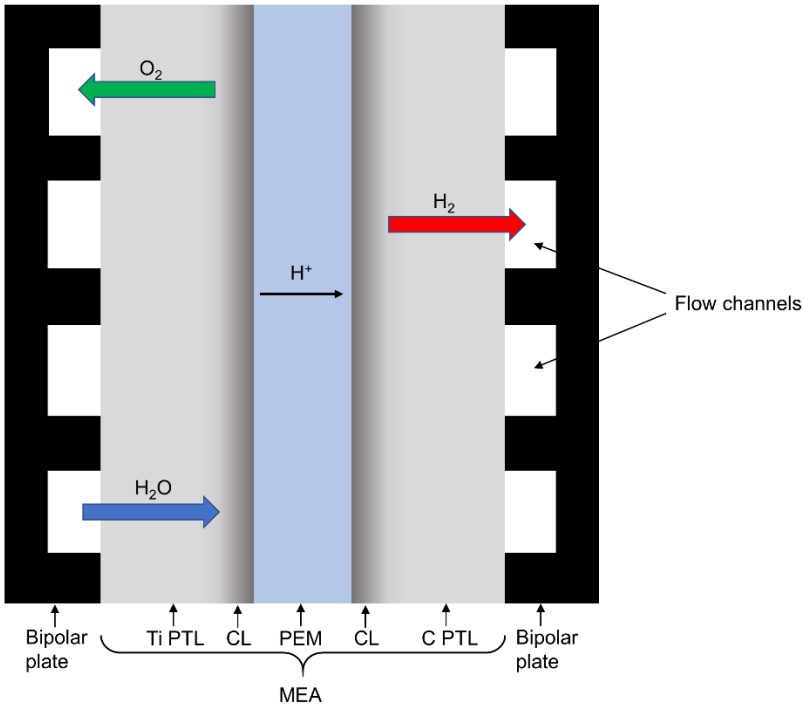

Figure 2: Schematic diagram of a PEM electrolyzer depicting the electrolyte membrane (PEM), catalyst layers (CLs), titanium and carbon porous transport layers (Ti PTL and C PTL), and bipolar plates which serve as supports for the flow fields. H_2O enters through the anode side and splits into O_2, protons and electrons. The protons go through the membrane and the electrons through an external circuit into the cathode where they combine to make H_2.

The function of PTLs is to supply water for electrolysis to the catalyst layer where the reaction takes place, remove product gases from the catalyst layer, conduct electricity, and transport heat[9]. Titanium (Ti) is the preferred material for PTLs employed in the anode side of PEM electrolyzers because it resists the corrosive environment that develops from operating at potentials above 1.23 V[12]. Porous sintered and fiber Ti PTLs are of interest in this work. Porous sintered Ti PTLs are made by irradiating powder Ti with a high-power laser[16]. Pore forming agents are added to the powder so that gas evolves at a designated temperature which creates the porous structure[16]. Therefore, the porosity and pore size can be adjusted when fabricating sintered Ti PTLs. Fiber Ti PTLs are made using weaving technology or pressing and sintering Ti fibers[17]. Fiber Ti PTLs usually have larger pore diameters and provide less contact with catalyst layer which lowers the electrochemical performance[17].

Like PTLs, GDLs serve similar functions in PEFCs. They supply the gases to the catalyst layers where the reaction takes place, remove product water from the catalyst layers, conduct electricity, and transport heat[18]. GDLs are made from carbon fibers that are made into nonwoven paper, woven cloth, or felt[18]. They have porosity ranging from 65 % to 90 %, thickness of 200 – 400 μm, and are treated with 5–20 % polytetrafluoroethylene (PTFE) and an MPL coating[10,18]. The MPL increases the contact between GDLs and catalyst layers while the PTFE adds hydrophobicity to the GDL system[12,18]. GDLs may experience temperature gradients over 5°C during operation in a PEMFC due to their high thermal resistance[18].

The porous flow-field in PEFCs and PEM electrolyzers is another component that is essential for transport. Porous flow fields with serpentine, maze or parallel flow configurations are usually machined onto graphite bipolar plates[13]. However, the weak flexural strength and brittleness of graphite make it unsuitable for transportation applications of PEFCs because vibrations and loading[13]. Open cell metal foams present good alternatives to graphite bipolar plates with machined flow channels. They can reach up to 95 % porosity, have good permeability

and distribute gas well[13]. Fabrication of open cell metal foams can be done by investment casting using a mold, electrolytic deposition, and chemical or physical vapor deposition on polymer templates[19]. The nickel chromium (NiCr) porous flow field studied in this work was made by way of electrolytic deposition. This method involves an anodic electrode being dissolved and deposited into a cathodic electrode that serves as a polymer template made conductive by sputtering or ionic deposition[19]. A subsequent electrolytic deposition of Ni or Cu is performed to create the metal foam[19].

Thermal management is necessary in fuel cells to maintain optimal operating temperatures and moisture content. Higher temperature operation improves reactions kinetics however[20], heat removal must be optimized because faster kinetics leads to larger heat production. Heat accumulation within the cell cause elevated temperatures that can degrade materials to the point of failure[10]. Furthermore, proton conductivity and activation overpotentials are affected by the temperature and moisture content in the membrane of PEFCs[20]. Nafion membranes will swell until it disintegrates at elevated temperatures and adequate access to water[20]. However, it can resist failure at elevated temperature with limited access to water. An increase in temperature causes drying which inhibits ion transport due to electro-osmotic drag. High temperatures and large thermal gradients contribute to degradation rates of fuel cells designed to function under specific conditions[20]. The GDLs in PEFCs account for one of the highest thermal resistances in the cell leading to thermal gradients and heat accumulation within the cell[18]. Therefore, GDLs' thermal properties should be a priority when optimizing thermal management of the overall PEFC.

An electrolyzer evolves oxygen and hydrogen from water molecules. This reaction is endothermic and therefore requires heat to proceed forward. The heat required must be transported to the reaction sites in the anode. Operating a PEM electrolyzer at increased temperatures reduce ohmic and activation losses due to increasing the ionic conductivity of the

membrane and faster reaction kinetics[9]. However, prolonged operation at elevated temperatures leads to degradation of cell components by way of membrane thinning and Ti PTL passivation that promotes gas crossover and increased contact resistance[21]. Therefore, a compromise between cell performance and durability must be made.

Thermal management is an important factor in the operation of PEFCs and PEM electrolyzers. The GDLs in PEFCs account for one of the highest thermal resistances in the cell leading to thermal gradients and heat accumulation within the cell[18]. PTLs within electrolyzers transport water to the anode catalyst layer and transfer heat among other functions. Flow field meshes distribute fluids which can aid in the removal or production of heat. The through-plane thermal conductivity of these components is investigated in this work experimentally *ex-situ* at room temperature and through modeling. Comparison of the two methods can lead to an understanding of the discrepancies between models and experimental results. Models are cost-effective and can predict temperature distribution and its effects on cells[9]. Additional information of thermal properties of materials can aid in adding parameters to models to make more accurate predictions of temperature distributions in PEFCs and PEM electrolyzers.

Thermal conductivity of transport layers and flow-field meshes have commonly been overlooked therefore this is still a growing field. As a result, the amount of information and references from which to compare is limited. The thermal conductivity of sintered Ti PTLs and GDLs with similar but not exactly the same properties to the samples studied in this work have been reported. Bock et. al.[9] reported the room temperature thermal conductivity of four different sintered Ti PTLs with porosity of 30.2 to 30.7 % at 5, 10, and 15 bar compaction pressure measured *ex-situ* with a similar experimental setup to this study. The thermal conductivities they measured were between 1.2 $Wm^{-1}K^{-1}$ and 1.7 ± 0.3 $Wm^{-1}K^{-1}$ for all four samples under dry conditions at a pressure of 5 bar. They also measured the thermal conductivity of one of the four different PTLs under wet conditions and reported a value of 7.2 ± 1.8 $Wm^{-1}K^{-1}$ at 5 bar compaction

pressure. The thermal conductivity increased by 0.1 to 0.3 $Wm^{-1}K^{-1}$ with increasing pressure. Mock et. al.[15] also reported the thermal conductivity of a sintered Ti PTL of 50 % porosity measured *in-situ* at 40°C, 65°C, and 90°C. The thermal conductivity was 8.61 $Wm^{-1}K^{-1}$, 8.72 $Wm^{-1}K^{-1}$, and 8.72 $Wm^{-1}K^{-1}$ at the temperatures listed above. They assumed that the PTL was dry while measuring, however, their values are more in agreement with the wet sample results reported in the aforementioned work by Bock et. al. Burheim et. al.[22] reported the room temperature thermal conductivity of a SIGRACET GDL 10 AA at 4.6, 9.3, and 13.9 bar compaction pressure also using a similar experimental setup. At 4.6 bar, they measured a thermal conductivity of 0.30 ± 0.02 $Wm^{-1}K^{-1}$ and 0.42 ± 0.04 $Wm^{-1}K^{-1}$ at 13.9 bar. This GDL has similar properties to the one measured in this work. To our knowledge, the thermal conductivity of the materials being measured in this work have not been reported.

The novelty of this work is in measuring of the through-plane thermal conductivity of materials for the first time. Chapter 1 of this work is the introduction which includes an overview of the importance of renewable energy, how PEFCs and PEM electrolyzers work, a description of PTLs, GDLs, and porous flow fields, and overview of the previous work relevant to the materials measured here. Chapter 2 is the methods and theory section, which introduces the underlying theory of this work, the experimental setup, equations for evaluation of data, experimental measurement method, description of the materials, and modeling. The experimental and modeling results are presented and discussed in Chapter 3. Finally, Chapter 4 is the conclusion summarizing this work.

2 METHODS AND THEORY

The thermal conductivity k is generally determined using Fourier's law

$$q" = -k\frac{\partial T}{\partial x} \quad (1)$$

where $q"$ is heat flux (heat rate per unit area) and $\frac{\partial T}{\partial x}$ is the one-dimensional temperature gradient. This equation describes heat transfer via conduction mechanism across a sample. Steady-state experimental methods are favored for determining thermal conductivity of materials because of their simplicity[23]. They require that a constant heat flux over time is applied to a sample of known dimensions. Figure 3 shows one-dimensional heat transfer through a medium and the linear relationship to temperature gradient at steady state. The temperature at T_1 and T_2 is measured while the constant heat flux is applied. Therefore, the thermal conductivity can be calculated using Eq. (1). It should be noted that for this method to be effective, the heat flux must be confined to one dimension. This means that all other sides of the sample require thermal insulation to minimize heat transfer in those directions.

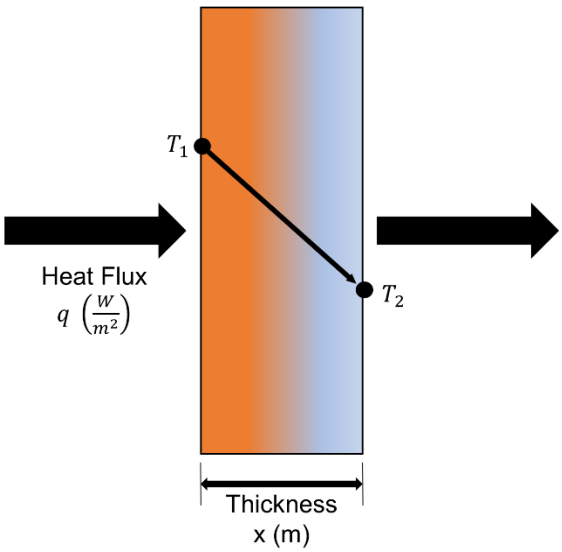

Figure 3: Representation of steady-state one dimensional heat transfer and temperature gradient across a sample of thickness x.

The thermal conductivity of PTL's, GDL's, and porous flow fields is experimentally determined *ex-situ* because it is difficult to measure thermal conductivity during fuel cell or electrolyzer operation. This is mainly because during operation heat is being generated inside the cell and needs to be accounted for. Measurements are done using the apparatus shown in Figure 4. It consists of two 2.54 cm diameter, 11.23 cm length 304 stainless steel cylinders of known thermal conductivity (14.4 $Wm^{-1}K^{-1}$) with aluminum tips to minimize radial temperature gradients along the surfaces in contact with the sample. Thermal paste is added between each metal to metal interface to decrease thermal contact resistance. The sample is placed between the cylinders and pressure is being applied, so that there is good contact between the surfaces. The thickness of the sample is measured with a micrometer located at the top of the apparatus. Heating blocks (Dabpress™ DIY uncaged press plates kit, Guangdong, China) are placed at the top to provide a constant heat flux and at the bottom is a heat sink through which cold water is supplied using an external water circulating bath (Cole-Parmer® Polystat® Cooling/Heating Circulating Bath, Vernon Hills , Illinois). The circulated water is necessary to provide a constant temperature boundary and to maintain a continuous heat flux through the apparatus thus preventing heat accumulation. The inlet water stream is insulated to maintain the cooling water temperature at the value set by Polystat, as it reaches the heat sink. Rectangular aluminum fins are fitted to the portion of the heat sink in contact with the bottom stainless steel cylinder to enhance convective heat transfer from the rod and into the circulating water. Each stainless-steel bar is fitted with four K type thermocouples equidistant from each other. The spacing between each thermocouple is between 3.72 cm and 3.75 cm. Thermocouples 1-3 and 6-8 measure the temperature at each point which is read out by a USB-TC data acquisition system. This gives the temperature gradient, which is then used to calculate heat flux through each stainless-steel bar using Fourier's law, Eq (1). The apparatus is insulated with 15 layers of ceramic fiber insulation sheets (McMaster-Carr 93285K22, Robbinsville, New Jersey) that are 1.59 mm thick each of thermal conductivity 0.067 $Wm^{-1}K^{-1}$ at 260°C according to manufacturer, to minimize radial heat

transfer and obtain a one-dimensional heat flux. Additionally, the setup is encased with acrylic sheet enclosure to prevent convective effects from the surroundings.

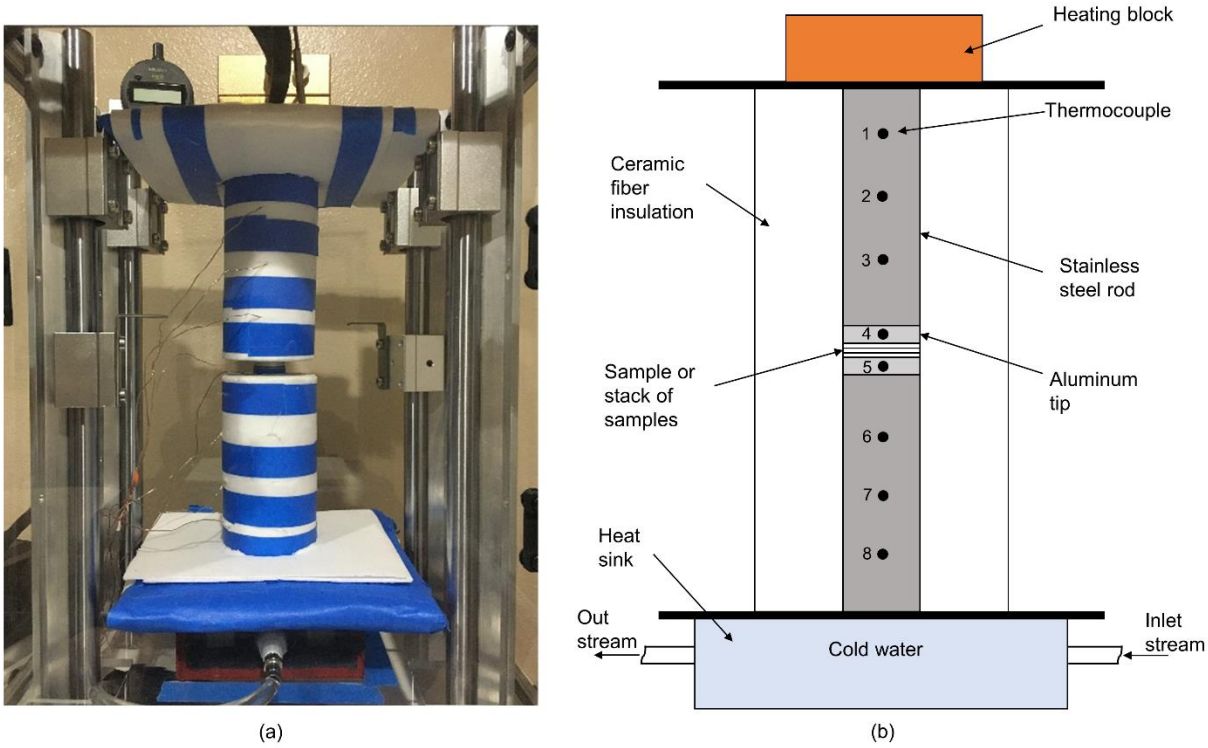

Figure 4: (a) Photograph of experimental setup and (b) schematic. The center portion of the setup is not insulated to show where the sample is placed. The schematic shows heating block, cold water bath, location and naming of eight thermocouples.

The thermal conductivity is measured indirectly by measuring the thermal resistance of stacked samples and their thickness. The heat flux through top and bottom rods is calculated with Fourier's law using the temperature measurements of thermocouples 1-3 and 6-8. The average is then taken to be the heat flux through the sample, since the thermal conductivity of stainless steel, k_{steel}, is known:

$$q"_{upper} = -k_{steel}\left(\frac{dT}{dx}\right)_{13} \quad (2)$$

$$q"_{lower} = -k_{steel}\left(\frac{dT}{dx}\right)_{68} \quad (3)$$

$$q"_{sample} = \frac{(q"_{upper} + q"_{lower})}{2} \quad (4)$$

Thermocouples 5 and 6 are used to calculate the total thermal resistance across the sample based on the sample heat flux defined here as,

$$R"_{total} = \frac{l}{k_{sample}} = \frac{(T_4 - T_5)}{q"_{sample}} \quad (5)$$

where l is the sample thickness. The total thermal resistance, $R"_{total}$ consists of the thermal contact resistance between the sample and the top surface, $R"_{Al\text{-}sample}$, the thermal resistance of the sample, $R"_{sample}$, and the thermal contact resistance between the sample and the bottom surface, $R"_{Al\text{-}sample}$, as shown in Figure 5.

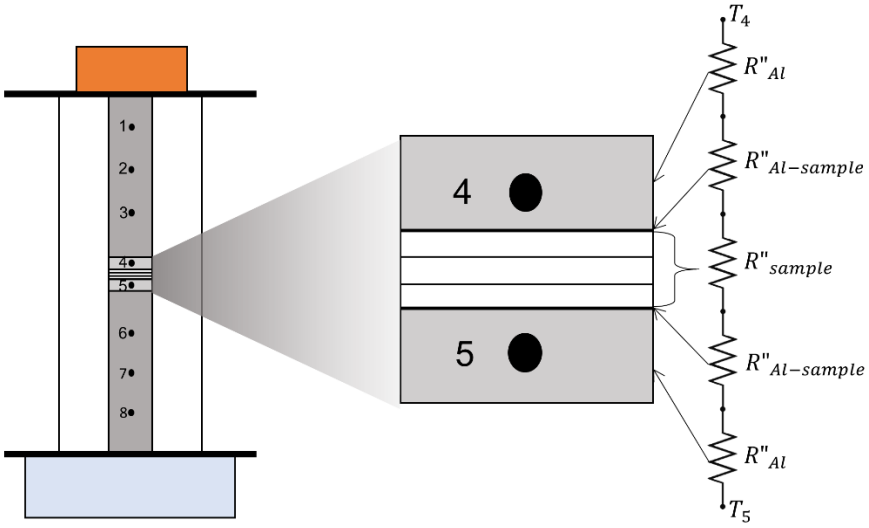

Figure 5: Equivalent circuit schematic for the thermal resistances that comprise the sample and the zoom-in schematic of the sample between two aluminum plates, where measured temperatures are T4 and T5.

Each stacked sample adds a thermal resistance to the system $R"_{sample-sample}$. However, Burheim et al.[11] demonstrated that the sample to sample thermal contact resistance is negligible. Also, the contribution from aluminum tips to thermal resistance are negligible due to Al high thermal conductivity, therefore $R"_{Al}$ are considered to be 0 here. Rearranging the sum of resistances leads to the following equation where $R"_{total}$, as shown in Eq. (5), has a dependence on the sample thickness.

$$R"_{sample} = R"_{total} - 2R"_{Al-sample} \quad (6)$$

Plotting the measured resistances of stacked samples calculated with Eq. (5) against their thickness effectively decouples the thermal conductivity and the contact resistances[11]. The inverse of the slope from this plot is the thermal conductivity of the sample and the intercept on y-axis is the contact resistances, $2R"_{Al-sample}$ (see Figure 6).

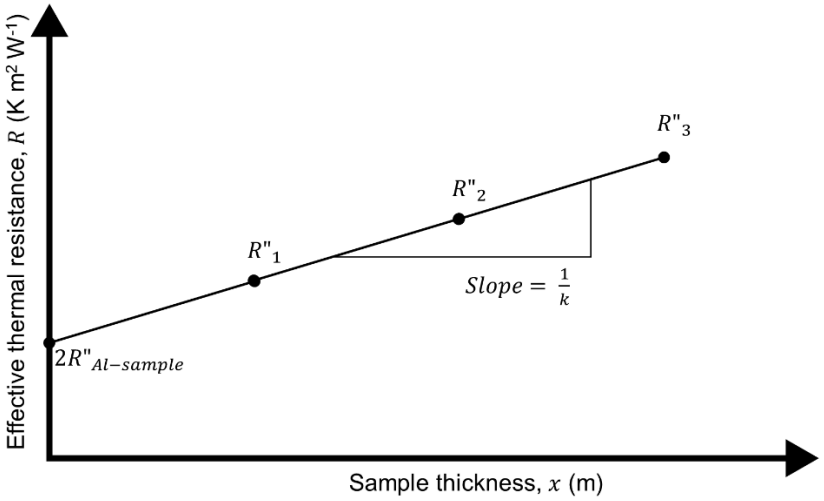

Figure 6: Example of plot of effective thermal resistance of 1, 2, and 3 layers of a sample, $R"_1$, $R"_2$, $R"_3$, respectively, against sample thickness.

2.1 Error Analysis

A statistical analysis was carried out to quantify the accuracy of the measurements in this study. The errors were quantified using variance and an analysis of error propagation[24]. The variance supplies a measure of spread of the collected sample data using the following equations

$$\bar{y} = \frac{\sum y}{n} \tag{7}$$

$$\sigma^2 = \frac{\sum (y-\bar{y})^2}{n-1} \tag{8}$$

in which $\bar{y}$ denotes the sample average and σ^2 is the sample variance, both based on a small sample of n observations. Taking the square root of the sample variance yields the sample standard deviation σ. The error in thermal conductivity is calculated with the standard deviation of the sample thermal resistance, heat flux, and thermal conductivity measurements.

$$\sigma_{k_{sample}} = \left|k_{sample}\right| \sqrt{\left(\frac{\sigma_{R"sample}}{R"sample}\right)^2 + \left(\frac{\sigma_{q"sample}}{q"sample}\right)^2} \tag{9}$$

Where $\sigma_{k_{sample}}$ is the error in thermal conductivity of the sample, $\sigma_{R"_{sample}}$ is the standard deviation of the sample resistance and determined from the results of Eq. (6), $\sigma_{q"_{sample}}$ is the standard deviation of the heat flux through the sample and is calculated as:

$$\sigma_{q"_{sample}} = \sqrt{\left(-k_{steel}\sigma_{\frac{dT}{dx}}\right)^2}$$

Where $\sigma_{\frac{dT}{dx}}$ is standard deviation in thermal gradient and is obtained by using the slope of the lines plotted in Figure 8b and Eq. (8).

2.2 Experimental

The samples are cut into 2.5 cm diameter circles with a punching tool and sometimes with scissors to fit between the top and bottom portions of the experimental setup. A single layer of the sample is sandwiched between the top and bottom cylinders making sure that it is centered. The center of the setup, between thermocouple 4 and 5 as shown in Figure 5,is reinsulated with 15 layers of insulating material to prevent radial heat transfer. The sample is compressed with the weight of the top bar and with additional 0.45 kgs. The heating blocks and the circulating water are set to the desired temperatures prior to data acquisition. Each experiment is run for 60 minutes to ensure that the system reaches steady state before taking final temperature readings for calculations. However, the samples with higher thermal resistance required an additional 20-30 minutes to completely stabilize. The temperature is plotted over time to verify that steady state is achieved before recording data. Figure 7shows the temperature readout (a) over the duration of one experiment for total of 65 minutes and (b) for five minutes after one hour to show that the system is at steady state. Fluctuations of less than 1 C per thermocouple are observed at this time.

The results presented by Burheim et al.[11] show that the thermal conductivity of Nafion membranes increased when wetted. Introduction of water is relevant, as fuel cells produce water and electrolyzers have water fed on the anode where PTLs are located. Therefore, the thermal conductivity of PTL was investigated in this work under dry and wet conditions.

The samples are assumed to be dry under room conditions and thus were left unchanged. The PTLs readily absorb water because they are hydrophilic. They are submerged in deionized water for 30 minutes at room temperature. When placed on the experimental setup, more water is added until the PTL layer is saturated. The center portion of the apparatus, shown in Figure 5, is wrapped with a thin layer of plastic to prevent water leakage from the sample. Afterwards, the same experimental procedure for the dry samples is implemented on the wetted samples. Since

three layers of the same material are available, the first measured layer is placed back into the deionized water after each experiment to maintain constant water saturation for subsequent experiments with more layers of the sample.

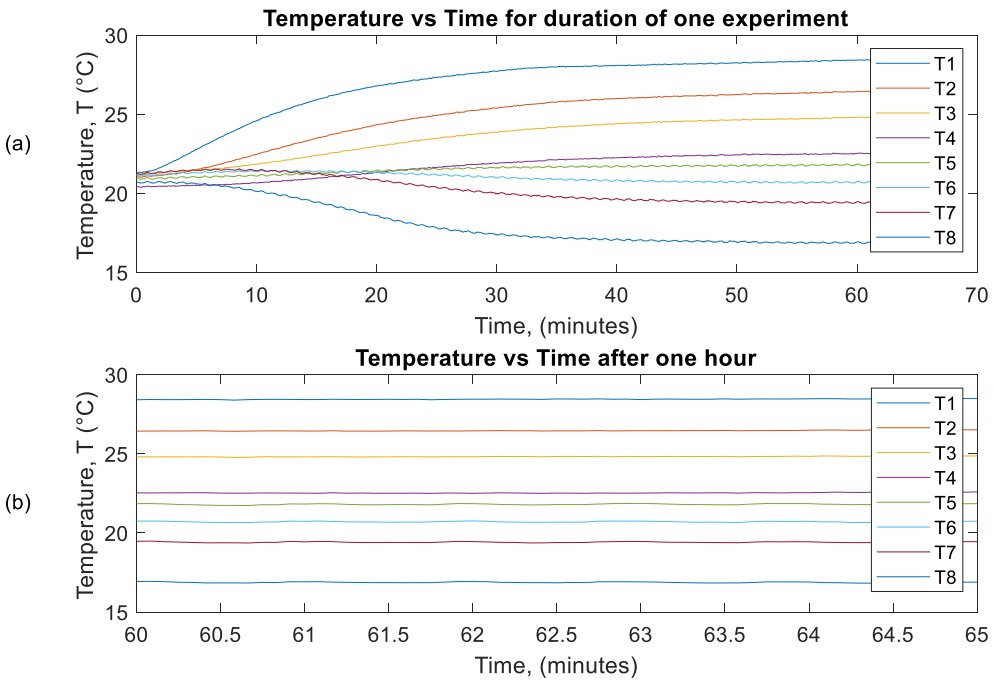

Figure 7: (a) Plot of temperature against time for one hour and five minutes and (b) for five minutes after one hour.

Temperature measurements are recorded with the eight thermocouples. The temperatures readings of thermocouples 1-3 and 6-8 are plotted against the distance between thermocouples within each set to calculate the temperature gradient dT/dx by way of linear regression. The effective thermal resistance is calculated using Eqs. (2-5). The overall procedure is repeated using 2 then 3 layers of the same sample. The thermal conductivity is obtained by

calculating the inverse of the slope of the line of resistance plotted against sample thickness as shown in Figure 6.

Effective thermal insulation in the radial direction is required to prevent heat transfer with the environment. About 15 layers of 1.59 mm ceramic fiber insulation was used on the top and bottom stainless steel rods. Without proper insulation, the high temperature region losses heat while the low temperature region absorbs heat since the temperatures are higher and lower than the surroundings, respectively. Consequently, a higher heat flux and lower temperature difference between the top and bottom surface of the sample is calculated. The thermal conductivity of the sample can result in values three times higher than the actual. Figure 8 is a graphical representation of the temperature gradients in the top and bottom cylinders of the apparatus. Fourier's law shows that heat flux and temperature gradient are linearly related, and for the same material, the temperature gradient should be the same. However, Figure 8(a) shows that the temperature gradients are not equal. The temperature gradient calculated with readings from thermocouples 1-3 is $-3.55℃\,cm^{-1}$ while the temperature gradient from thermocouples 6-8 is $-1.70℃\,cm^{-1}$. Heat was lost as it was transferred through the cylinders radially. Figure 8(b) shows equal temperature gradients through the top and bottom portions of $-0.27℃\,cm^{-1}$ and $-0.28℃\,cm^{-1}$, respectively, which is the expected trend if heat loss is minimal.

These radial heat diffusion effects were minimized by increasing the thickness of the insulation and by decreasing the temperature range between the top and the bottom of the apparatus. The temperature range that achieved the best results was from 12°C to 35°C. The difference in temperature from thermocouple to thermocouple is 1°C to 2°C at this range. Therefore, the thermocouples must be calibrated so that the readout is the same for a surface of known temperature. The DAQ software auto calibrates but the thermocouples were also tested using the heating blocks to ensure they all read the same temperature. Additionally, the thermocouples are sensitive therefore bending the wires or poor thermal contact affects the

temperature readouts. Since the cylinders are insulated, it was assumed that the temperature through them is the same when no heat flux is supplied. Temperature measurements were taken without an applied heat flux on the apparatus to test whether the thermocouples worked properly and registered the same temperature.

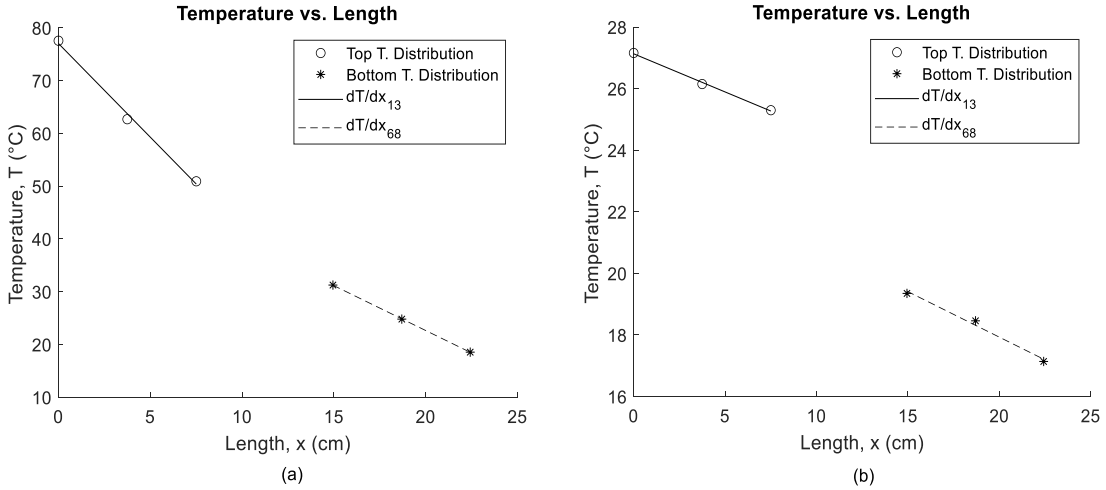

Figure 8: Temperature distribution plot when (a) heating block temperature is 100°C with five layers of insulation and (b) heating block temperature is 35°C with fifteen layers of insulation. The x-axis represents the length along the entire setup with thermocouple 1 starting at x = 0.

2.3 Materials

Five different materials were tested using the experimental setup in Figure 4: polyether ether ketone (PEEK), sintered titanium PTL (NEL Hydrogen, Wallingford, CT), fiber titanium PTL, nickel-chromium ceramic metal (Sumitomo), and AvCarb GDS2185 (AvCarb Material Solutions, Lowell, Massachusetts). PEEK is an insulating material with a highly stable chemical structure which makes it chemically inert. This material is used to validate the results obtained with our apparatus and the experimental procedure because of its well-known properties. The thermal

conductivity of PEEK was calculated under different conditions to determine optimal operating conditions of the apparatus. The PEEK samples (McMaster-Carr, Robbinsville, New Jersey) were cut using a micro milling machine to a diameter of 2.5 cm from a sheet of 0.2 cm thickness. The thermal conductivity of two PTLs with different morphologies are studied here; a sintered titanium PTL and a fiber titanium PTL as shown in Figure 9. Titanium is the preferred material for PTLs in PEM electrolyzers because of its resistance to the corrosive environment found in the anode that results from operating potentials above 1.23 V[9,12]. The sintered titanium PTL thickness measurements were 0.258 mm, 0.255 mm, and 0.257 mm. For the fiber titanium, the measurements were 0.267 mm, 0.266 mm, and 0.268 mm. The nickel-chromium ceramic metal is used as a porous flow field in PEM fuel cells. Porous flow fields distribute the fuel and oxidant to the catalyst layer where the reactions occur[13]. The nickel chromium layers measured 0.533 mm, 0.532 mm, and 0,544 mm .The titanium PTLs and nickel-chromium samples were outlined using a 2.5 cm circular punch and cut from a single sheet of sintered titanium PTL, fiber titanium PTL, and nickel-chromium porous material. A metal file was used to round the edges to minimize heat transfer effects along the circumference. The thermal conductivity of the two PTLs and porous flow field were investigated under dry and wet conditions. The gas diffusion layer AvCarb GDS2185 is made from polytetrafluoroethylene (PTFE) treated carbon fiber paper with a microporous layer coating on one side. A publicly available technical data sheet that includes mechanical properties is available on the AvCarb Material Solutions website. A 2.5 cm circular punch was used to cut the desired number of samples from a single sheet of GDS2185 with thickness measurements of 0.239 mm, 0.241 mm, and 0.242 mm. The samples along with their thickness and purpose are tabulated in Table 1.

Table 1: Materials tested using our experimental setup

Sample	Average Layer thickness	Purpose
PEEK (polyetheretherketone)	2.03 mm	Validation of experimental setup
Sintered Ti	0.257 mm	Electrolyzer PTL
Fiber Ti	0.267 mm	Electrolyzer PTL
NiCr celmet	0.536 mm	Fuel cell porous flowfield
GDS2185	0.241 mm	Fuel cell GDL

2.4 Modeling

The following modeling procedure was adapted from Leonard et al. in which tomographic images were obtained at Advanced Light Source (ALS) at Lawrence Berkeley National Laboratory (LBNL)[12]. The samples were rotated 180° to generate a three-dimensional image with the x-ray tomography scans. The duration of each scan lasted no longer than 30 minutes with one field of view collected per sample. The images were generated with a 1.3 μm voxel resolution having 3.3 mm horizontal field of view. The thermal conductivity of the sintered and fiber titanium PTLs, porous flow field, and gas diffusion system GDS2185 was also calculated by simulation with a 3-D model. The important parameters for calculating the effective thermal conductivity are solid volume fraction and tortuosity as shown in the following equation:

$$k_{effective} = \frac{\varepsilon}{\tau}\ k_{bulk} \tag{10}$$

here, ε is the solid volume fraction, τ is the tortuosity, $k_{effective}$ is the effective thermal conductivity and k_{bulk} is the thermal conductivity of the bulk material. The solid volume fraction is computed by thresholding images obtained with X-ray CT and calculating the ratio of solid volume to total volume. The tortuous pathways within a porous material are described by the tortuosity, which is defined as actual length of transport divided by geometric length. It was calculated using the

MatLab application TauFactor which allows through plane and in plane analysis. The area perpendicular to the through plane direction was modeled as 1 mm^2 for both PTLs and 1.3 mm x 1.6 mm for the GDS. Through-plane tortuosity was obtained, as this is the one that is relevant to the through-plane calculations of effective conductivity. Further information of sample morphology is provided by analysis of porosity and pore size distribution (PDS). The following figures show the dimensions of the samples and visual representation of their morphologies. Figure 9 shows the 3D computer-generated images of the sintered and fiber titanium PTLs demonstrating the differences in morphology and solid volume fraction.

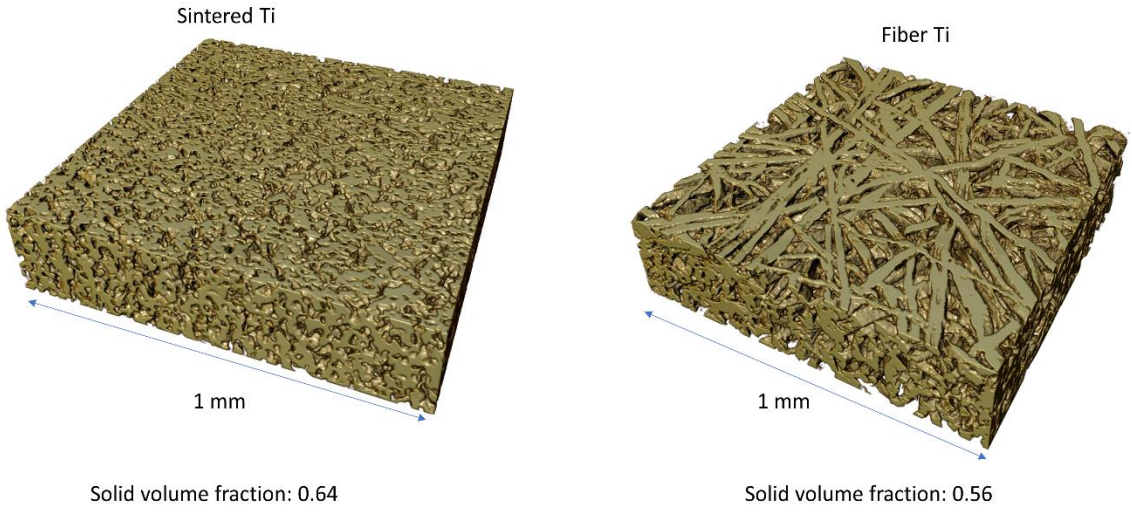

Figure 9: 3D rendering of sintered and fiber Ti PTL samples.

Sintered Ti had solid volume fraction of 0.64, whereas Fiber Ti had solid volume fraction of 0.56. Figure 10(a) is a volume-rendered representation nickel-chromium ceramic metal and Figure 10(b) is a cross-section tomograph of a single slice.

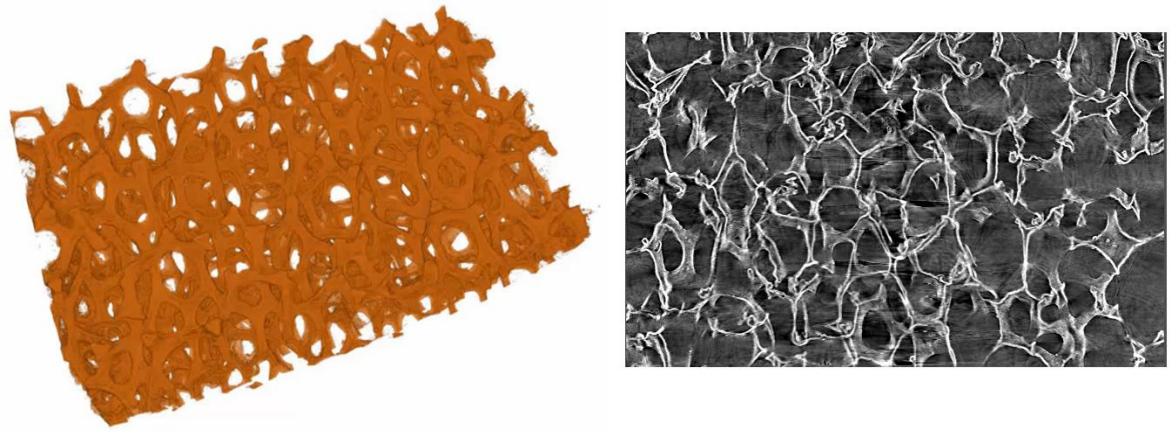

Figure 10: (a) 3D rendering and (b) surface image of nickel-chromium ceramic metal.

Figure 11 and Figure 12 provide through-plane, inplane and volume-rendered images of GDS2185 along with the different components present its structure. Figure 11 shows how each component, MPL, fiber, and binder, looks and how they are layered. MPL is present only on one side of the material, whereas carbonaceous binder is present throughout the sample. The MPL is partially free-standing and a small fraction of MPL is embedded into the GDL.

Figure 12 presents information on porosity as a function of GDL thickness, power density function as a function of radius, and 3D rendering on the GDL as a whole. The pore-size distribution is bimodal with larger pores having average radius of 8.4 µm, whereas smaller pores have the radius of 4.3 µm. The non-uniform through-thickness porosity reflects the presence of MPL on one side of the GDL and the binder that is more present on the surfaces of the GDL, leaving the center of the GDL to be the most porous.

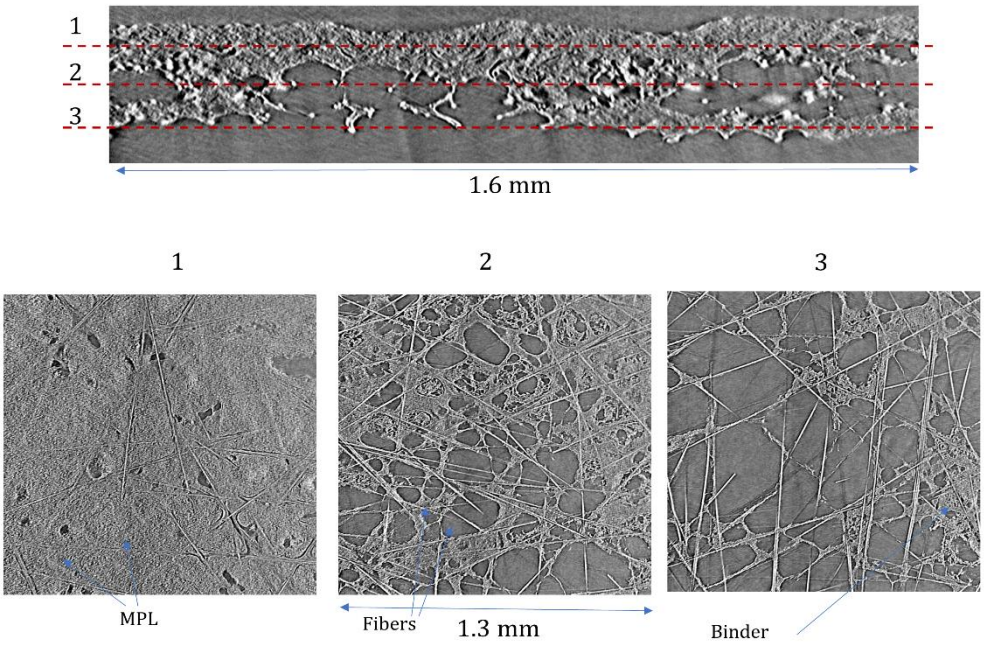

Figure 11: Images of GDS2185 from three directions showing the materials it is composed of along with their placement.

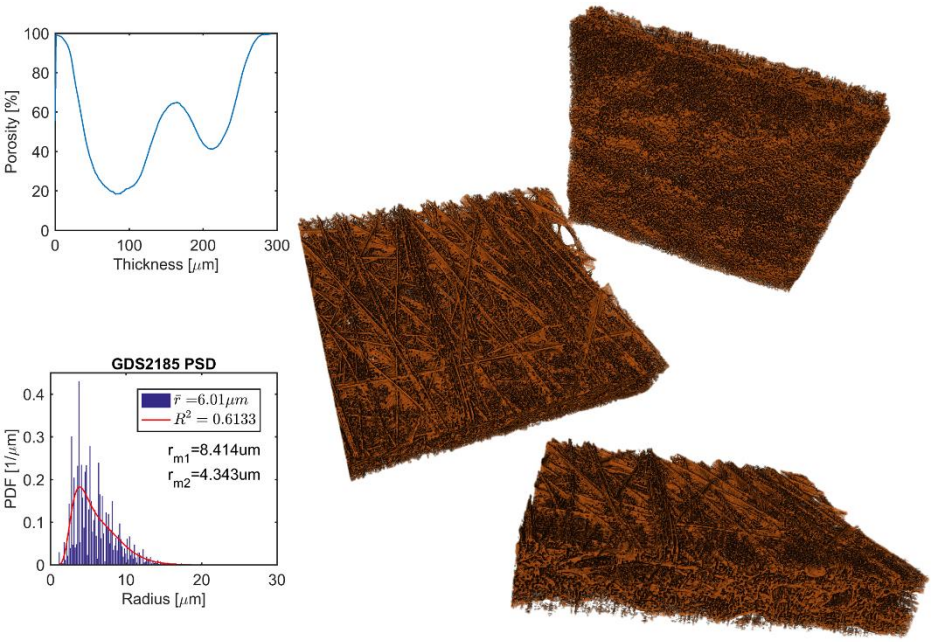

Figure 12: 3D rendering of GDS2185 along with plots relating porosity with thickness and power density function (PDF) with radius.

3 RESULTS

3.1 Method Validation

To validate the experimental method and apparatus, experiments were first done on layers of PEEK. Experiments were performed until optimal operating conditions were obtained. The actual thermal conductivity of PEEK as reported by the manufacturer, McMaster-Carr, is 0.25 $Wm^{-1}K^{-1}$. Initial measurements yielded results as high as 0.778 W $m^{-1}K^{-1}$ when 5 layers of insulation were used on stainless steel rods with heating block temperature set to 48.9°C and circulating water set to 5°C. Increasing the amount of insulation to 10 layers while maintaining the same heating block and circulating water temperature resulted in a thermal conductivity of 0.550 $Wm^{-1}K^{-1}$. The change in the result due to increasing insulation suggests that heat losses were present during the experiment under these conditions. A thermal conductivity of 0.394 $Wm^{-1}K^{-1}$ was achieved by increasing insulation to 15 layers along with a decrease in heating block temperature to 35°C.

The difference in thermal conductivity with increasing insulation is because the heat exchange with the environment is limited especially in the upper section of the setup. With lower insulation, the thermal gradient measured with thermocouples 1-3 is higher because heat is lost as the it travels from one point to another. Therefore, the temperature measured by thermocouple 3 is lower because of the heat loss and leads to the higher thermal gradient. In the lower section of the experimental setup, from thermocouple 6 to 8, thermocouple 6 measures a higher temperature because of the heat gained. Heat gain, in upper section, and heat loss, in lower section, do not seem to affect the temperature of thermocouple 1 and 8 to the same extent as 3 and 6. This observation is likely due to thermocouple 1 being located close to the heat source and 8 close to the heat sink. The thermal gradients measured under these conditions result in a heat flux that has been affected by radial heat exchange, therefore it is higher than the actual heat flux going through the sample. When insulation was increased from 5 to 10 layers, the heat flux in the

upper section measured for one PEEK insert decreased from 984 Wm^{-2} to 917 Wm^{-2}, for two inserts it decreased from 850 Wm^{-2} to 777 Wm^{-2}, and for three inserts from 872 Wm^{-2} to 748 Wm^{-2}. Eq. (5) shows that heat flux is inversely proportional to thermal resistance and proportional to thermal conductivity.

Figure 13 shows the progression in thermal conductivity measurements as experimental conditions are changed. Ultimately, increasing the circulating water temperature to 13°C while maintaining the heating block temperature of 35°C gives values similar to the one reported by manufacturer. This is because one wants to minimize temperature difference between the top and bottom of the stainless-steel rods and to keep the average temperature close to that of ambient air. Under these conditions the heat loss to environment will be minimized. Figure 14 shows a plot of the effective thermal resistances and thermal conductivity calculated from the temperature measurements. The inverse of the slope of the lines in Figure 14(a) is the thermal conductivity of the sample and the y-intercept is the thermal contact resistance. The thermal conductivities were 0.28 ± 0.03 $Wm^{-1}K^{-1}$ and 0.28 ± 0.03 W $m^{-1}K^{-1}$ and the contact resistance, $2R_{Al-sample}$, was 0.0029 Km^2W^{-1} and 0.0033 Km^2W^{-1} for PEEK for two different trials. Changing the operating temperatures decreases the heat flux and thus the amount of heat loss radially to the environment. Measurement of PEEK thermal conductivity compared to the value reported by manufacturer has 12-13 % of error. This required lower heat flux through the system and adequate insulation.

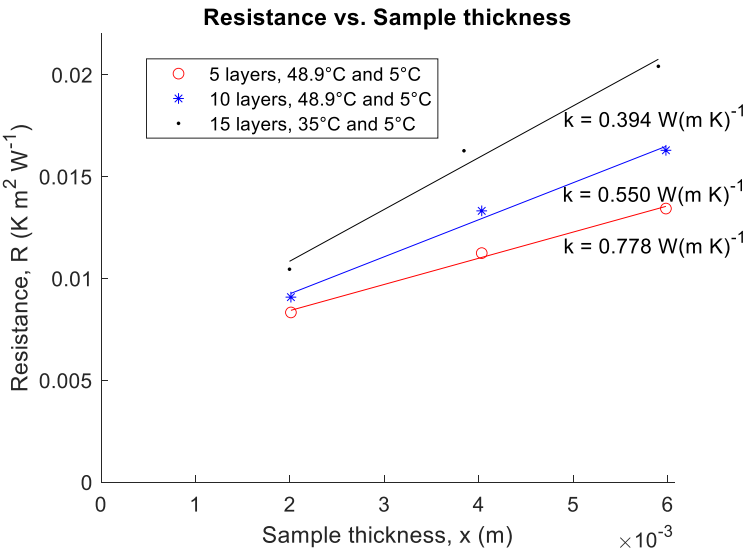

Figure 13: Plot of effective thermal resistances under different conditions showing that increasing insulation and reducing the heat flux increases the accuracy of measurements.

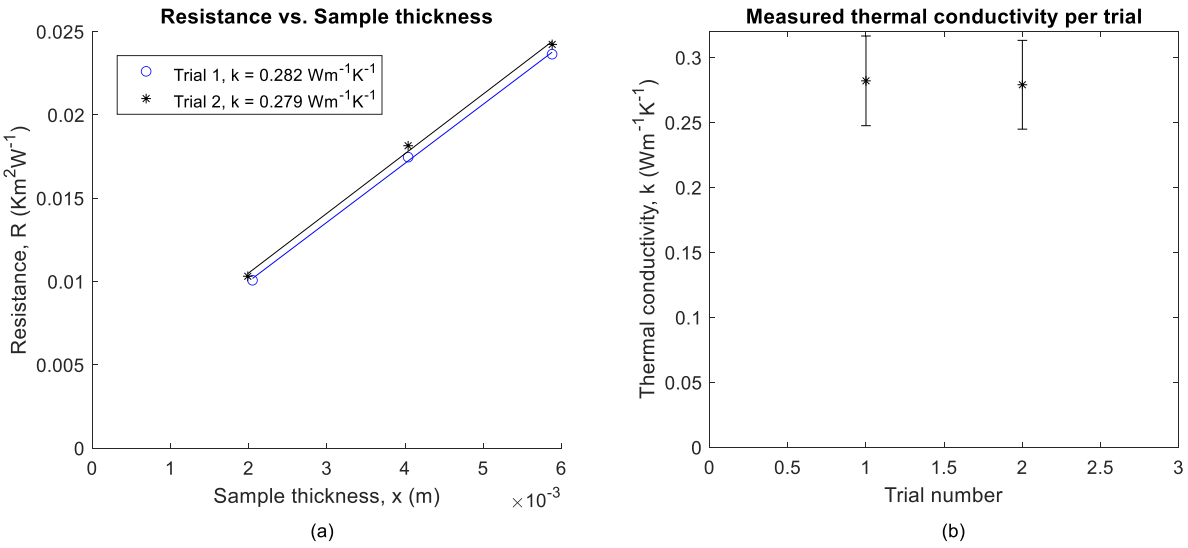

Figure 14: Plot of (a) thermal resistance against thickness and (b) thermal conductivity with error margins for two experiments using PEEK. Each point represents one layer of sample. Fifteen layers of insulation were used and operating temperature of the heating block and circulating water were 35°C and 13°C, respectively.

The main contributor to error propagation was the differences in the thermal gradients from the top and bottom stainless steel rods and fluctuations in heat flux due to thermal gradient. With more trials and data, the error values will decrease, evident by the Eq. 8 which shows that standard deviation is inversely proportional to the number of trials. Therefore, the standard deviation and error would decrease with more trials.

3.2 Sintered and fiber Ti PTLs

3.2.1 Modeling Results

The thermal conductivity of the sintered and fiber Ti PTL samples was investigated through modeling using the MatLab application TauFactor. Results are shown in Figure 15 alongside maps of the structure and temperature distribution. Of importance is the tortuosity and solid volume fraction because these values are used to calculate the effective thermal conductivity of the sample based on the bulk thermal conductivity and the structure of the material. The tortuosity describes the tortuous path through which heat is transferred in porous materials. In this case, it is a ratio of the actual length heat travels divided by the straight-line length of the sample. Therefore, the length of heat transfer in a material affects the thermal conductivity by reducing it depending on how tortuous the path is.

The model shows that the sintered Ti PTL has a solid volume fraction of 64 % and tortuosity of 1.42. The thermal conductivity of bulk titanium is 17 $Wm^{-1}K^{-1}$ and using Eq. 10, the thermal conductivity of the sintered Ti PTL is calculated to be 7.66 $Wm^{-1}K^{-1}$. The solid volume fraction and tortuosity of the fiber Ti PTL are 56.2 % and 1.83, respectively. Figure 16 shows the results for the fiber Ti PTL. The thermal conductivity is calculated to be 5.22 $Wm^{-1}K^{-1}$. The thermal conductivity of sintered and fiber Ti decreased by 55 % and 69 %, respectively, compared to the bulk. The fiber Ti is more porous than the sintered Ti therefore it is expected to have a lower

thermal conductivity. The voids within the sample decrease the thermal conductivity, therefore, a higher void volume leads to lower thermal conductivity.

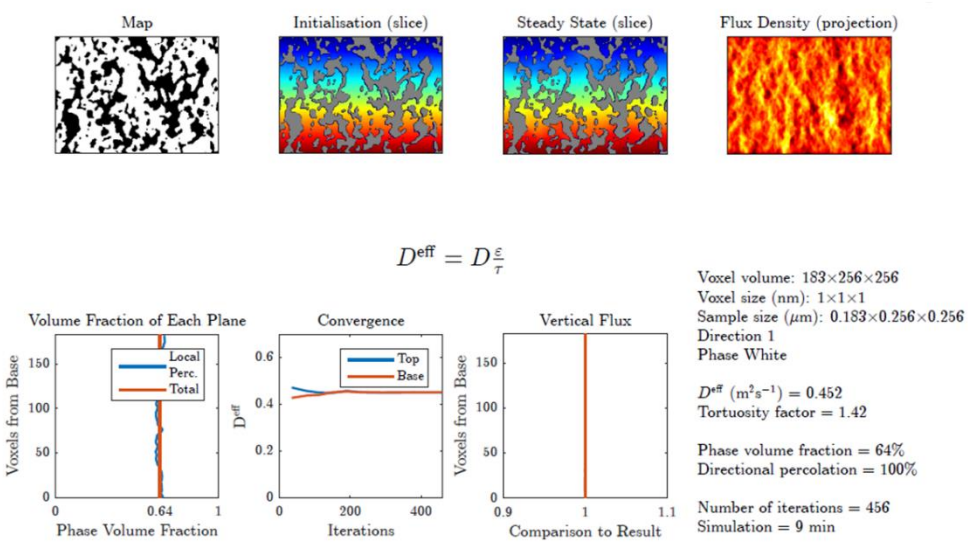

Figure 15: Modeling results using TauFactor for sintered Ti PTL sample.

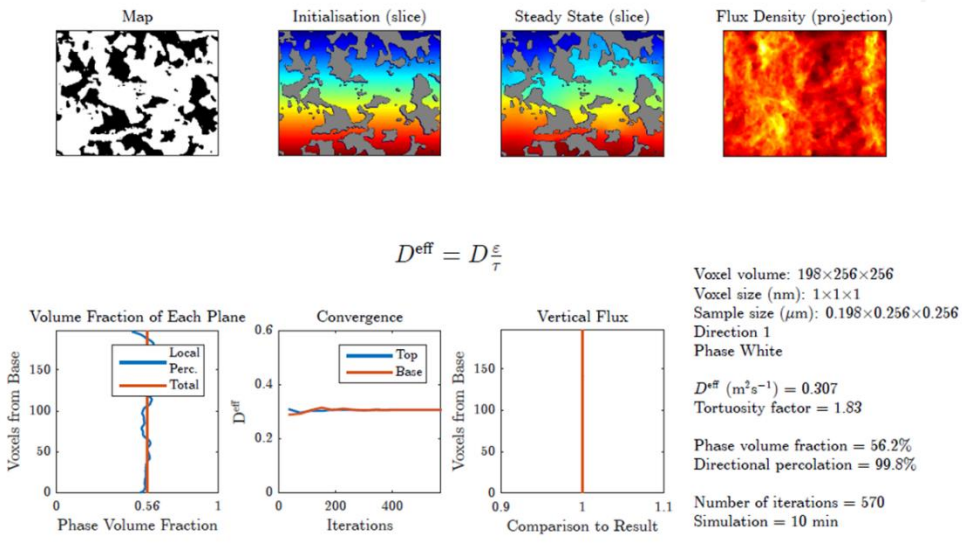

Figure 16: Modeling results using TauFactor for fiber Ti PTL sample.

3.2.2 Experimental Results

The thermal conductivity of sintered and fiber titanium PTL's was also measured experimentally under dry and wet conditions. Figure 17 shows three measurements of the resistances of 1, 2, and 3, layers of the sintered Ti sample. Although the thermal resistance measurements for each set of layers differs, the slope of the slope of the fitted line for each trial is similar and results in similar thermal conductivity. The thermal conductivity, k, calculated for these trials is 0.48 ± 0.22 $Wm^{-1}K^{-1}$, 0.45 ± 0.21 $Wm^{-1}K^{-1}$, and 0.44 ± 0.20 $Wm^{-1}K^{-1}$. The thermal contact resistance for trial 1, 2, and 3 is 0.0014 Km^2W^{-1}, 0.0009 Km^2W^{-1}, and 0.0008 Km^2W^{-1}, respectively. The differences in the values of the thermal resistances plotted in Figure 17 are due to the differences in the temperature gradients and the temperature fluctuations during data acquisition. The temperature gradients ranged from 31°Cm^{-1} to 51°Cm^{-1}.

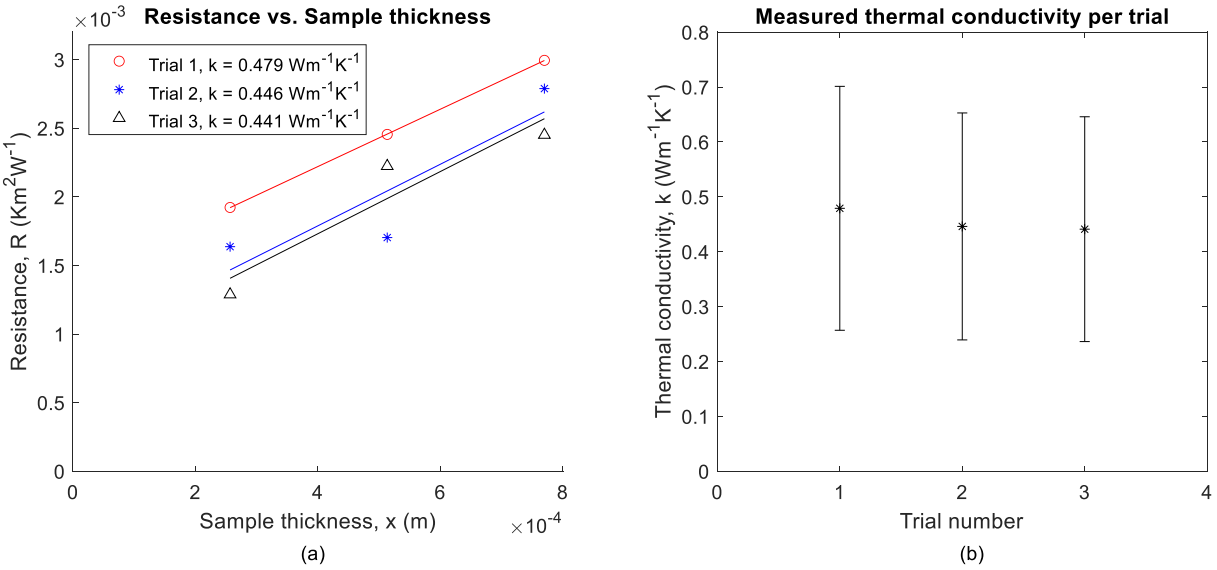

Figure 17: Plot of (a) effective thermal resistance against thickness and (b) effective thermal conductivity with error margins for three measurements of sintered Ti PTL samples.

Bock et. al. reported a thermal conductivity of 1.6 $Wm^{-1}K^{-1}$, 1.9 $Wm^{-1}K^{-}1$, and 2.2 $Wm^{-1}K^{-1}$ for sintered Ti with 30.3 % porosity under 5 bar, 10 bar, and 15 bar pressure[9]. The thermal conductivity of the sample here is expected to be lower because it has a higher porosity of 36 % and was not measured under applied pressure. The thermal conductivity increases with increasing pressure and decreases with increasing porosity.

The thermal conductivity of the sintered Ti PTL doubled when wetted with DI water. The sintered Ti PTLs did not show swelling, therefore no modifications to their dimensions was necessary. Figure 18 shows three measurements of the resistances of 1, 2, and 3, layers of the wet sintered Ti PTL sample. The thermal resistance measurements with 1 layer differ the most for the experiments with the wetted sintered Ti PTL. The thermal conductivity, k, calculated is 0.9 8 ± 0.11 $Wm^{-1}K^{-1}$, 0.88 ± 0.10 $Wm^{-1}K^{-1}$, and 0.87 ± 0.10 $Wm^{-1}K^{-1}$. The thermal contact resistance for trial 1, 2, and 3 is -3E-06 $Km^{2}W^{-1}$, -7E-05 $Km^{2}W^{-1}$, and -8E-05 $Km^{2}W^{-1}$, respectively. These values are unphysical as thermal contact resistance should be a positive value. The negative values for thermal contact resistance might be due to the thermal resistance measurement of 3 stacked layers of the sample. The thermal resistance might have been slightly inflated because of a lower water content within 3 layers compared to 1 and 2 layers. Experiments with 3 layers of sample probably experienced more saturation loss due to the higher amount of water required to saturate the samples with each increase in thickness.

The sintered Ti PTL samples was observed to absorb water rapidly which is expected due to its hydrophilic nature. However, some of the water would leak when the samples were pressed between the top and bottom rods. More detailed measurements with exact water content measurements are needed to develop a relationship between thermal conductivity and water content. Furthermore, the negative intercept might be due to the fact that the samples were drying out during the experiment.

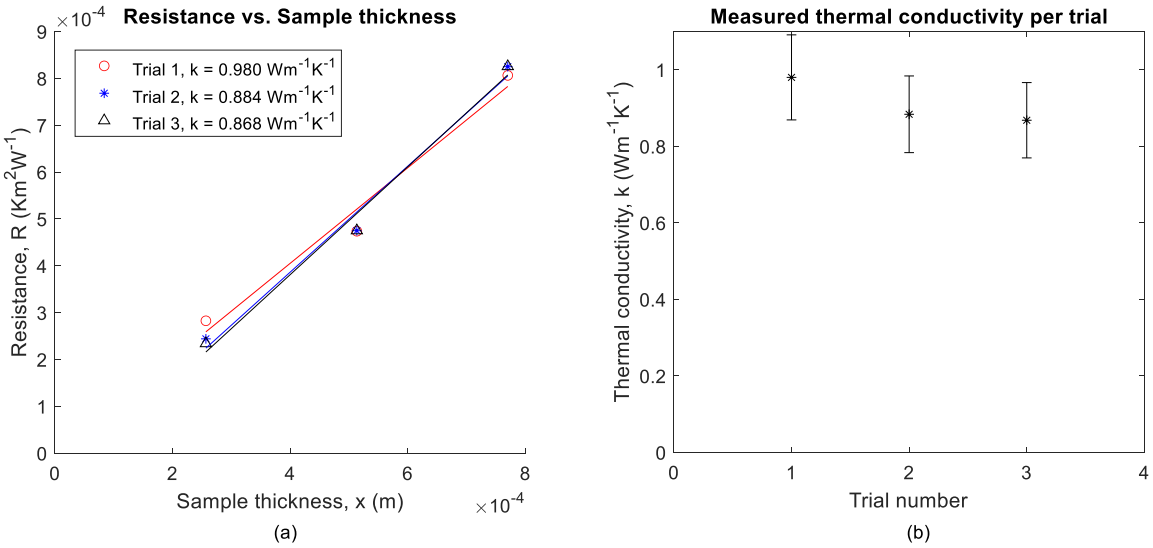

Figure 18: Plot of (a) effective thermal resistance against thickness and (b) effective thermal conductivity with error margins for three measurements of sintered Ti PTL samples wetted with DI water.

The measured effective thermal conductivity of the fiber Ti PTL sample is 0.43 ± 0.07 $Wm^{-1}K^{-1}$, 0.43 ± 0.07 $Wm^{-1}K^{-1}$, and 0.39 ± 0.06 $Wm^{-1}K^{-1}$ with thermal contact resistance 0.0009 Km^2W^{-1}, 0.0012 Km^2W^{-1}, and 0.0011 Km^2W^{-1} for trial 1, 2, and 3, respectively, under dry conditions. A plot of the total resistance as a function of sample thickness is shown in Figure 19. The measured thermal resistances of the first trial differ from trial two and three, however the slopes of the fitted lines are similar, resulting in consistent thermal conductivity.

The average effective thermal conductivity is 9 % lower than that of the sintered Ti PTL. This result is expected due to the higher porosity and modeled results of the fiber Ti PTL. The contact resistances for fiber Ti PTL sample are slightly higher than those for sintered Ti PTL samples. This is expected, as fiber Ti PTL has lower overall contact area with aluminum plate and between the layers compared to sinter Ti PTL (which has higher solid volume fraction). The plot

in Figure 19 has similar features to Figure 17. This is also due to the temperature fluctuations and differences in temperature gradients from trial to trial.

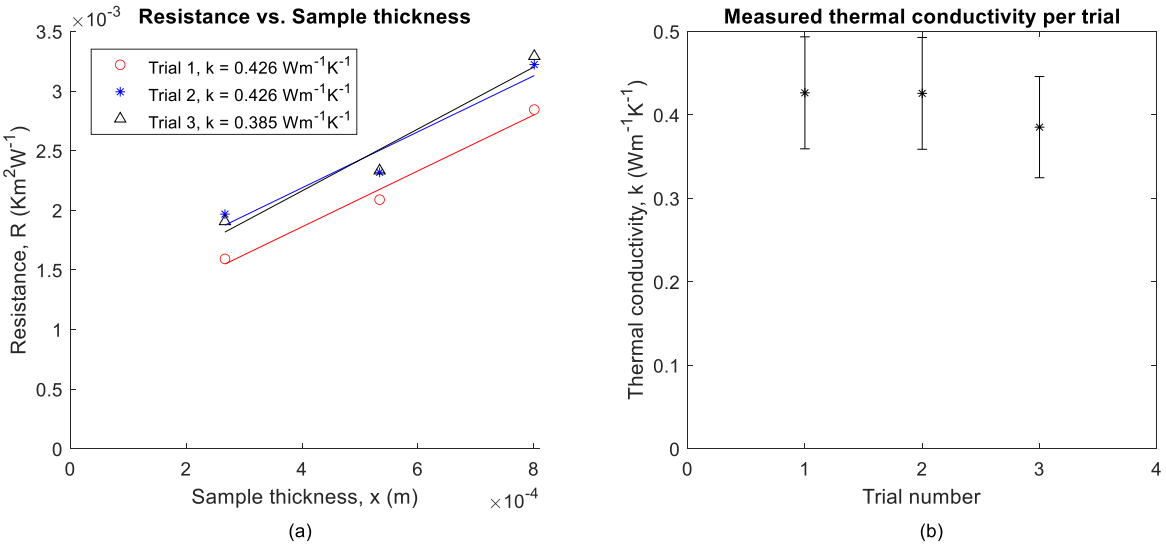

Figure 19: Plot of (a) effective thermal resistance against thickness and (b) effective thermal conductivity with error margins for three measurements of fiber Ti PTL samples.

Adding DI water to the fiber Ti PTL increased the effective thermal conductivity as it did in the sintered Ti PTL. Figure 20 shows the thermal resistances plotted against sample thickness. The thermal conductivity of the wetted fiber Ti PTL for three measurements is 0.76 ± 0.44 $Wm^{-1}K^{-1}$, 0.79 ± 0.46 $Wm^{-1}K^{-1}$, and 0.80 ± 0.46 $Wm^{-1}K^{-1}$ with thermal contact resistance -.0003 Km^2W^{-1}, -.0003 Km^2W^{-1}, and -.0002 Km^2W^{-1}, respectively.

Similarly, to wetted sintered Ti PTL the thermal contact resistances are negative, which is unphysical. The effective thermal conductivity of the wetted fiber Ti PTL sample is still lower than that of the wetted sintered Ti PTL. It is again, expected as introduction of water should not change the ratio of thermal conductivities between these materials. Based on these results, the sintered Ti PTL has higher effective thermal conductivity and is better at reducing heat losses within an

electrolyzer. Consequently, higher temperature within the catalyst layer would enhance reaction kinetics and ion transport.

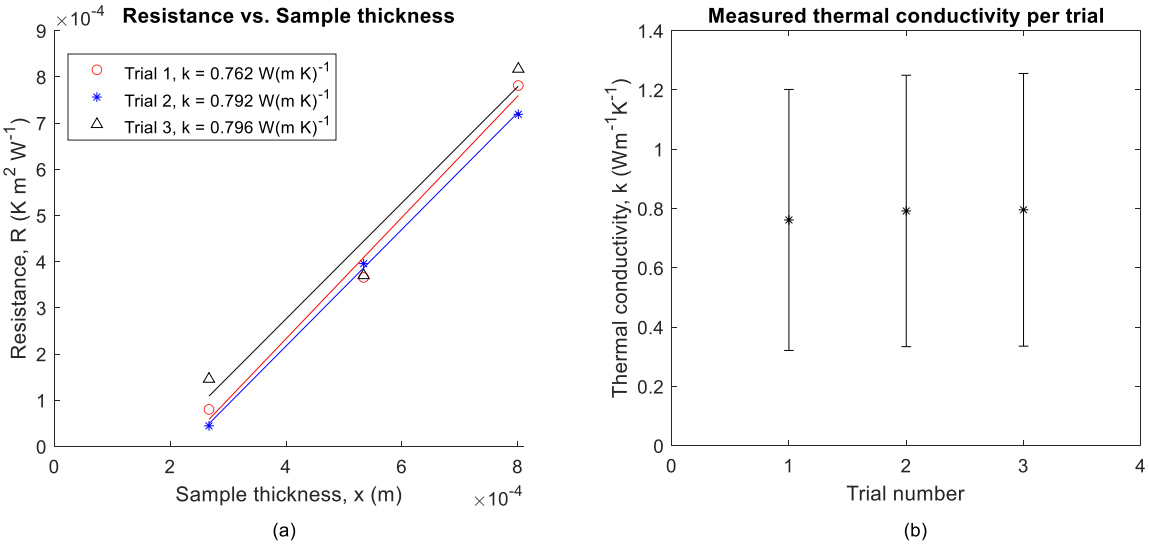

Figure 20: Plot of (a) effective thermal resistance against thickness and (b) effective thermal conductivity with error margins for three measurements of fiber Ti PTL samples wetted with DI water.

The experimental and modeling results show that the thermal conductivity of the sintered Ti PTL is higher than that of the fiber Ti PTL by 1.12 and 1.47, respectively. However, the effective thermal conductivity calculated using the model versus the experimental differ for both samples. The experimental effective thermal conductivity for the sintered Ti PTL is 16.7 times lower than those from the model and 13.4 times lower for the fiber Ti PTL. Table 2 lists the effective thermal conductivity for the fiber and sintered Ti PTLs under dry conditions, wet conditions, and from the model. The difference between the model and experimental results can be attributed to the ideal nature of the model where effects from grain boundaries and titanium dioxide formation on the surface of Ti are not present. Grain boundaries decrease the thermal conductivity of polycrystalline materials such as metals. Ihlefeld et. al.[25] studied the effects of grain size and

porosity on the thermal conductivity of $SrTiO_3$ thin films. They reported that thermal conductivity has a strong dependence on grain size and porosity. Their findings show that the effect was greater for their porous sample. Additionally, a thin layer of titanium dioxide forms on the surface of titanium which protects it from corrosion. A porous titanium material would therefore have more titanium dioxide than bulk titanium. Titanium dioxide has lower thermal conductivity than titanium, therefore, it would also decrease thermal conductivity. The effective thermal conductivity of the dry samples was calculated experimentally and through a simulated model to compare the results. The values calculated using the model overshoots the effective thermal conductivity of the PTLs because nonidealities are not considered.

To compare the results of the wet sintered and fiber Ti PTLs, the thermal conductivity is calculated analytically based on a parallel layer arrangement of conduction, where heat conducts in parallel through the PTL and water. The total thermal resistance of parallel resistors is calculated by:

$$\frac{1}{R_{tot}} = \frac{1}{R_{PTL}} + \frac{1}{R_w} \tag{11}$$

where R_{tot} is the total thermal resistance of the sample, R_w is the thermal resistance of water, and R_{PTL} is the effective thermal resistance of the PTL. Using the definition of resistance, $R = L/kA$, substituting the area of the PTL material and of water with the total area multiplied by the porosity, $A_{PTL} = A_{tot}\varepsilon$ and $A_w = A_{tot}(1-\varepsilon)$, and cancelling terms gives:

$$k_{tot} = k_{PTL}\varepsilon + k_w(1-\varepsilon) = k_{PTL,eff} + k_w(1-\varepsilon) \tag{12}$$

where k_{tot} is the total thermal conductivity of the wet sample, $k_{PTL,eff}$ is the measured effective thermal conductivity of the Ti PTL sample, fiber and sintered, k_w is the thermal conductivity of water, and ε is the solid fraction. Eq. (12) shows that the total thermal conductivity is the sum of component thermal conductivities when modeled as a parallel circuit. The measured effective

thermal conductivity of the PTL, $k_{PTL,eff}$, is used here for $k_{PTL}\varepsilon$ because the calculation is based on the measurement of the dry sample to compare it to the wet sample. $k_{PTL,eff}$ is appropriate here because it is specific to the material and morphology that makes up the sample. Additionally, the thermal conductivity contribution of air at room temperature, 0.025 $Wm^{-1}K^{-1}$, within the sample is assumed to be negligible. The thermal conductivity of the wet samples is calculated to be 0.68 $Wm^{-1}K^{-1}$ and 0.73 $Wm^{-1}K^{-1}$ for the sintered and fiber Ti PTLs, respectively, using Eq. (12) and is used to compare the effective thermal conductivity of the wet samples calculated experimentally. The measured effective thermal conductivity was 1.3 times that of the predicted value for the wet sintered Ti PTL and 1.1 times for the wet fiber Ti PTL. Bock et. al. reported that the thermal conductivity of wetted 33 % porosity sintered Ti PTL samples increased by 4.3 times of the dry samples[9]. The same increase in not observed here, however, their measurements were taken over a period of 20 minutes whereas the wet samples in this work were measured for 65 minutes or more if the temperatures were not yet stable. The deviations in wet sample thermal conductivities compared to literature are likely due to effects from water saturation. This is a preliminary study on the effect of water on thermal conductivity of Ti PTLs and exact measurements of water saturation in the sample are not available here or, to our knowledge, in literature. We suspect that some of the water contained within the samples leaked by this time because visible water was not observed on the surfaces of the sample upon removal. This leads us to believe that residual water between the fibers or particles is the main contributor to the increase in thermal conductivity. Shum et. al. reported thermal conductivity measurements of a wet SGL10BA GDL in which experiments were done for 250 minutes[18]. The thermal conductivity they measured was about two times that of the dry GDL which is similar to the increase observed here. Although the water in their samples had evaporated, the thermal conductivity remained almost constant. This is mainly due to the fact that residual water wetted the contact between the

fibers and increased thermal conductivity. A similar effect is seen here, evident by the difference between measured and predicted thermal conductivity values for the wet samples.

In all the measurements, the sintered Ti PTL has a higher effective thermal conductivity than the fiber Ti PTL. The fiber sample has a higher porosity, as shown in the 3D renderings and modeling results in section 3.2.1., which leads to a lower amount of thermal contacts from which to conduct heat. Therefore, difference in effective thermal conductivity between fiber and sintered Ti PTLs stems from the morphology of the materials.

Table 2: Tabulated experimental and modeled thermal conductivity results for sintered and fiber Ti PTL's. Experimental values presented are averaged.

	Thermal conductivity	
Method	Sintered Ti PTL ($Wm^{-1}K^{-1}$)	Fiber Ti PTL ($Wm^{-1}K^{-1}$)
Experimental (dry)	0.46 ± 0.21	0.41 ± 0.07
Experimental (wet)	0.91 ± 0.10	0.78 ± 0.46
Model	7.66	5.22

3.3 NiCr celmet

Experimental thermal resistance and thermal conductivity measurements are plotted in Figure 21. The thermal conductivity measured for each linearly fitted set of data is 0.15 ± 0.03 $Wm^{-1}K^{-1}$, 0.18 ± 0.04 $Wm^{-1}K^{-1}$, and 0.17 ± 0.03 $Wm^{-1}K^{-1}$ with thermal contact resistance 0.0016 Km^2W^{-1}, 0.0021 Km^2W^{-1}, and 0.002 Km^2W^{-1} for trials 1, 2, and 3, respectively. The measured thermal resistance with three layers differs the most as seem in Figure 21(a). However, it does not cause a large difference in the measured thermal conductivity. The thermal conductivity of the NiCr porous flow field sample was the lowest compared to the PTL's and the GDL. The structure

of this sample is more porous than the others and thus experiences a larger decrease in thermal conductivity. Furthermore, the thermal contact resistances are the highest for NiCr celmet compared to the PTLs, as they have the lowest metal area in contact with aluminum plate.

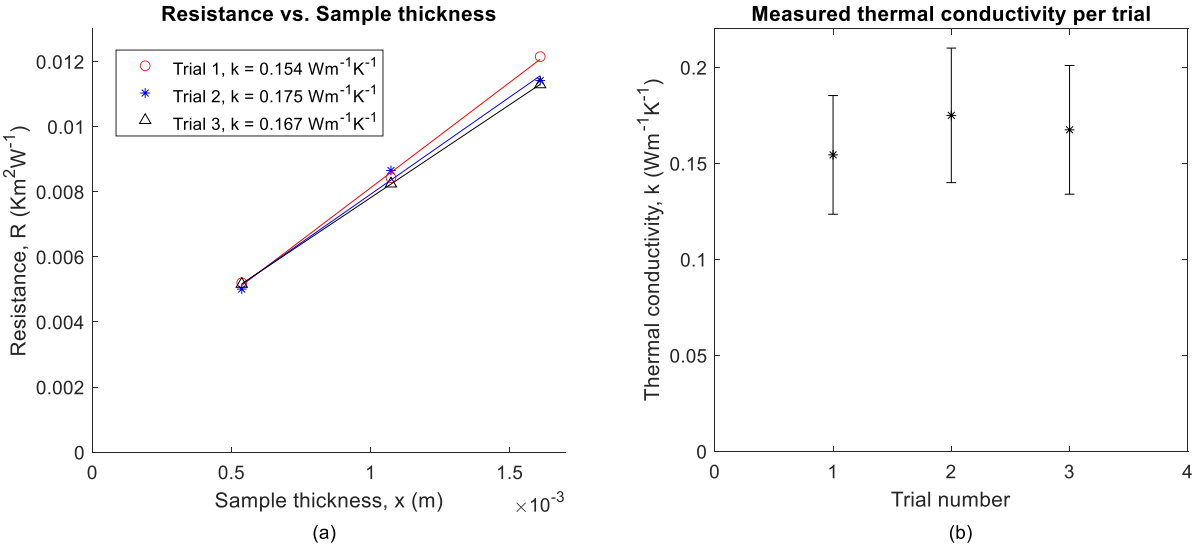

Figure 21: Plot of (a) thermal resistance against thickness and (b) thermal conductivity with error margins for three measurements of NiCr celmet flow field samples.

3.4 GDL - AvCarb GDS2185

Figure 22 shows the results of thermal resistance and thermal conductivity measurements in plots (a) and (b), respectively. The measured thermal conductivity of the GDL sample is 0.27 ± 0.04 $Wm^{-1}K^{-1}$, 0.32 ± 0.05 $Wm^{-1}K^{-1}$, and 0.37 ± 0.06 $Wm^{-1}K^{-1}$ with thermal contact resistance 0.0002 Km^2W^{-1}, 0.0003 Km^2W^{-1}, and 0.0005 Km^2W^{-1} for trial 1, 2, and 3, respectively. The thermal resistance measurement of three layers in trial one differs the most as shown in Figure 22(a).This measurement seems to expand the thermal conductivity range of the GDL the most, however the results are equally spaced from 0.27 $Wm^{-1}K^{-1}$ to 0.37 $Wm^{-1}K^{-1}$. The thermal conductivity of AvCarb

GDS2185 has not been measured before but this GDL has properties similar to the ones of the SIGRACET GDL.

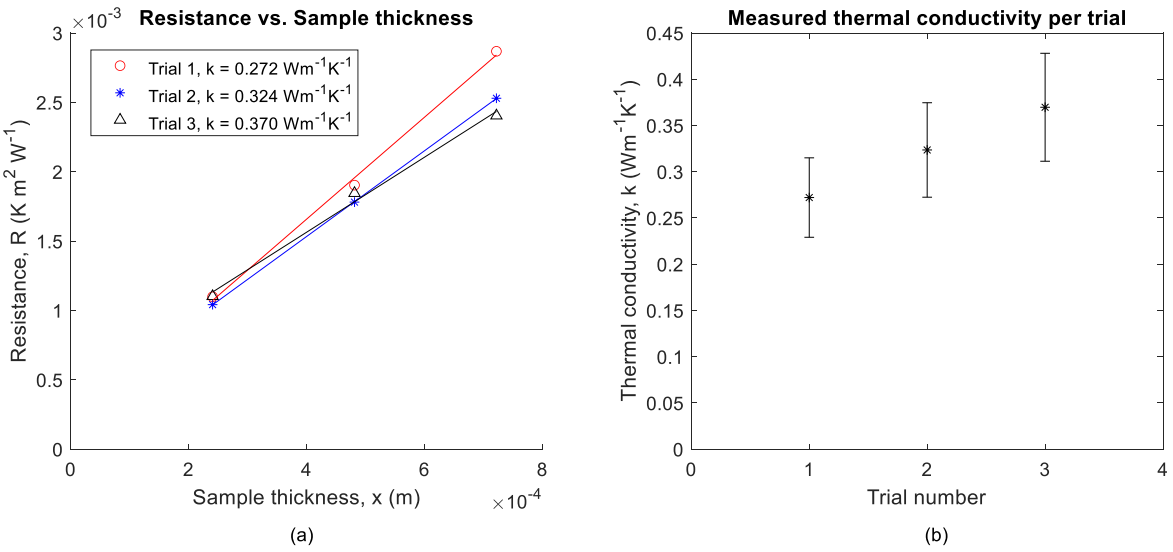

Figure 22: Plot of (a) thermal resistance against thickness and (b) thermal conductivity with error margins for three measurements of GDL samples.

Burheim et. al. measured the thermal conductivity of a SIGRACET GDL with no PTFE content and one with 5 wt% PTFE[22]. At 4.6 bar compaction pressure, the thermal conductivities reported are 0.30 $Wm^{-1}K^{-1}$ and 0.26 $Wm^{-1}K^{-1}$ for the GDL with no PTFE and with 5 wt%, respectively. The thermal conductivity increases by 0.03-0.08 $Wm^{-1}K^{-1}$ as pressure is increased. The thermal conductivity values observed for the AvCarb GDL is well within the range reported for the SIGRACET GDL 10 AA[22].

Based on the results presented here, the thermal conductivity measured experimentally for the sintered Ti PTL is the highest, followed by the fiber Ti PTL, GDL, and NiCr porous flow

field material in descending order. **Table 3** shows the values obtained experimentally and through a model for the materials tested.

Table 3: Tabulated thermal conductivity values for the materials measured experimentally and modeled.

Material	**Thermal conductivity experimental (**$Wm^{-1}K^{-1}$)	**Thermal conductivity Model (**$Wm^{-1}K^{-1}$)
Sintered Ti PTL	0.46 ± 0.21	7.66
Sintered Ti PTL (wet)	0.91 ± 0.10	
Fiber Ti PTL	0.41 ± 0.07	5.22
Fiber Ti PTL (wet)	0.78 ± 0.46	
NiCr porous flow field	0.17 ± 0.03	
AvCarb GDS2185	0.32 ± 0.05	

4 CONCLUSION

The effective thermal conductivity of sintered and fiber Ti PTLs, a GDL, and a NiCr porous flow field mesh is measured indirectly from thermal resistance of stacked layers of each individual material. These materials are relevant to PEFCs and PEM electrolyzers. They are key components in thermal management and can aid in the optimization of fuel cell and electrolyzer systems. Thermal conductivity of transport layers has generally been overlooked but in recent years efforts to optimize thermal management of fuel cells and electrolzyers motivated some researchers to pick up the topic.

In this work, Fourier's Law was employed as the basis of analysis. Therefore, the important parameters are heat flux, thermal gradient, and thermal conductivity. The measurements are done using an experimental setup built inhouse. It is designed to measure the heat flux through the system and the temperature difference through the samples which are used to calculate the thermal resistance. The effective thermal conductivity of dry and wet samples is calculated from slope of a line fitted through a plot of thermal resistances against length. Ti PTLs were measured under dry and wet conditions. Additionally, volume rendered X-ray tomography is used to understand the structure of the samples, subsequently allowing the calculation of effective thermal conductivity of these porous layers.

The thermal conductivity of the PTLs calculated using tomography results is 16.7 and 13.4 times higher than the values measured experimentally for the dry sintered Ti PTL and fiber Ti PTL, respectively. The effective thermal conductivity of the dry sintered and fiber Ti PTLs is 0.46 ± 0.21 $Wm^{-1}K^{-1}$ and 0.41 ± 0.07 $Wm^{-1}K^{-1}$. The difference between experimental and tomography aided values may be because of the ideal nature of the model which does not consider effects from grain boundaries or oxide layer formation. Furthermore, the experimental thermal conductivity results of the wet PTLs was higher than what calculations using a parallel resistor circuit predicts. We believe that the higher thermal conductivity is due to increased fiber to fiber

contact by residual water within the samples. When comparing literature values of other sintered Ti PTLs, it was found that the thermal conductivities here differ. However, the values that have been reported are for PTLs with different porosity and possibly different structural features. The thermal conductivity of the AvCarb GDL had not been measured in literature before. However, its morphological properties have similarities with SIGRACET GDL 10 AA. The thermal conductivity of 0.32 ± 0.05 $Wm^{-1}K^{-1}$ measured here agrees with previously reported values of the SIGRACET GDL 10 AA. Finally, the effective thermal conductivity of the NiCr porous flow field mesh is 0.17 ± 0.03 $Wm^{-1}K^{-1}$. The NiCr mesh has the highest porosity among the samples measured here and resulted in having the lowest thermal conductivity.

The differences in thermal conductivity of PTLs along with the lack of literature data to compare illustrates the importance of measuring thermal properties of transport layers and flow fields. More work is necessary in the characterization of thermal properties of these materials. Future work involves studying the effect of compaction pressure on the thermal conductivity of these materials. Furthermore, it is important to study the effects of water saturation on these materials in more detail because water is present in fuel cells and electrolyzers. Preliminary experiments on the effects of water on thermal conductivity are done here and show that the presence of water increases the thermal conductivity.

REFERENCES

1. Saeedmanesh, A., Mac Kinnon, M. A. & Brouwer, J. Hydrogen is essential for sustainability. *Curr. Opin. Electrochem.* **12**, 166–181 (2018).

2. Brouwer, J. Hydrogen and Fuel Cells for Zero Emissions Ohio Fuel Cell Symposium. (2019).

3. Gahleitner, G. Hydrogen from renewable electricity: An international review of power-to-gas pilot plants for stationary applications. *Int. J. Hydrogen Energy* **38**, 2039–2061 (2013).

4. Burheim, O. S., Su, H., Hauge, H. H., Pasupathi, S. & Pollet, B. G. Study of thermal conductivity of PEM fuel cell catalyst layers. *Int. J. Hydrogen Energy* **39**, 9397–9408 (2014).

5. Buttler, A. & Spliethoff, H. Current status of water electrolysis for energy storage, grid balancing and sector coupling via power-to-gas and power-to-liquids: A review. *Renew. Sustain. Energy Rev.* **82**, 2440–2454 (2018).

6. Carmo, M., Fritz, D. L., Mergel, J. & Stolten, D. A comprehensive review on PEM water electrolysis. *Int. J. Hydrogen Energy* **38**, 4901–4934 (2013).

7. Koumi Ngoh, S. & Njomo, D. An overview of hydrogen gas production from solar energy. *Renew. Sustain. Energy Rev.* **16**, 6782–6792 (2012).

8. O'Hayre, R. P., Cha, S.-W., Colella, W. G. & Prinz, F. B. *Fuel Cell Fundamentals*. (John Wiley & Sons, Inc., 2016).

9. Bock, R. *et al.* Measuring the thermal conductivity of membrane and porous transport layer in proton and anion exchange membrane water electrolyzers for temperature distribution modeling. *Int. J. Hydrogen Energy* **45**, 1236–1254 (2020).

10. Bock, R. *et al.* Thermal Conductivity and Compaction of GDL-MPL Interfacial Composite Material. *J. Electrochem. Soc.* **165**, F514–F525 (2018).

11. Burheim, O., Vie, P. J. S., Pharoah, J. G. & Kjelstrup, S. Ex situ measurements of through-plane thermal conductivities in a polymer electrolyte fuel cell. *J. Power Sources* **195**, 249–256 (2010).

12. Leonard, E. *et al.* Interfacial analysis of a PEM electrolyzer using X-ray computed tomography. *Sustain. Energy Fuels* **4**, 921–931 (2020).

13. Awin, Y. & Dukhan, N. Novel Flow Field for Proton Exchange Membrane Fuel Cells Made from 72%-Porous Aluminum Foam. *Procedia Comput. Sci.* **158**, 163–168 (2019).

14. Alhazmi, N. E. Thermal Conductivity of Proton Exchange Membrane Fuel Cell Components. (The University of Leeds, 2014).

15. Möckl, M., Bernt, M., Schröter, J. & Jossen, A. Proton exchange membrane water electrolysis at high current densities: Investigation of thermal limitations. *Int. J. Hydrogen Energy* **5**, (2019).

16. Yun, H. J. *et al.* Fabrication of porous titanium parts by powder bed fusion of Ti-TiH2 blended powder. *J. Mater. Res. Technol.* (2020) doi:10.1016/j.jmrt.2020.01.033.

17. Hackemüller, F. J., Borgardt, E., Panchenko, O., Müller, M. & Bram, M. Manufacturing of Large-Scale Titanium-Based Porous Transport Layers for Polymer Electrolyte Membrane Electrolysis by Tape Casting. *Adv. Eng. Mater.* **21**, 1–10 (2019).

18. Shum, A. D. *et al.* Investigating Phase-Change-Induced Flow in Gas Diffusion Layers in Fuel Cells with X-ray Computed Tomography. *Electrochim. Acta* **256**, 279–290 (2017).

19. Queheillalt, D. T., Hass, D. D., Sypeck, D. J. & Wadley, H. N. G. Synthesis of open-cell metal foams by templated directed vapor deposition. *J. Mater. Res.* **16**, 1028–1036

(2001).

20. Pharoah, J. G. & Burheim, O. S. On the temperature distribution in polymer electrolyte fuel cells. *J. Power Sources* **195**, 5235–5245 (2010).

21. Frensch, S. H. *et al.* Influence of the operation mode on PEM water electrolysis degradation. *Int. J. Hydrogen Energy* **44**, 29889–29898 (2019).

22. Burheim, O. S., Pharoah, J. G., Lampert, H., Vie, P. J. S. & Kjelstrup, S. Through-plane thermal conductivity of PEMFC porous transport layers. *J. Fuel Cell Sci. Technol.* **8**, 1–11 (2011).

23. Roos, M. M. & Weber, A. Z. Forschungspraktikum Parametric Studies on Through-Plane Thermal Conductivity of Gas Diffusion Layers for PEM-Fuel Cells Parametrische Studien zur Wärmeleitfähigkeit von Gasdiffusionsschichten für PEM-Brennstoffzellen. (2014).

24. Box, G. E. P., Hunter, J. S. & Hunter, W. G. *Statistics for Experimenters*. (John Wiley & Sons, Inc., 2005).

25. Ihlefeld, J. F., Brown-Shaklee, H. & Hopkins, P. E. Grain size and porosity effects on the thermal conductivity of SrTiO 3 thin films. 1–3.